AGU PUBLICATIONS

Geophysical Research Letters

RESEARCH LETTER
10.1002/2014GL061855

Key Points:
- A new full-wave anisotropic tomography is applied to Southern California
- The multiscale inversion achieves naturally data-adaptive spatial resolutions
- Spatial variations of anisotropy correlate well with tectonic features

Supporting Information:
- Readme
- Figure S1
- Figure S2
- Figure S3
- Figure S4
- Figure S5

Correspondence to:
Y.-P. Lin,
f97224204@ntu.edu.tw

Citation:
Lin, Y.-P., L. Zhao, and S.-H. Hung (2014), Full-wave multiscale anisotropy tomography in Southern California, *Geophys. Res. Lett.*, *41*, 8809–8817, doi:10.1002/2014GL061855.

Received 16 SEP 2014
Accepted 29 OCT 2014
Accepted article online 8 DEC 2014
Published online 23 DEC 2014

Full-wave multiscale anisotropy tomography in Southern California

Yu-Pin Lin[1,2], Li Zhao[2], and Shu-Huei Hung[1]

[1]Department of Geosciences, National Taiwan University, Taipei, Taiwan, [2]Institute of Earth Sciences, Academia Sinica, Taipei, Taiwan

Abstract Understanding the spatial variation of anisotropy in the upper mantle is important for characterizing the lithospheric deformation and mantle flow dynamics. In this study, we apply a full-wave approach to image the upper-mantle anisotropy in Southern California using 5954 SKS splitting data. Three-dimensional sensitivity kernels combined with a wavelet-based model parameterization are adopted in a multiscale inversion. Spatial resolution lengths are estimated based on a statistical resolution matrix approach, showing a finest resolution length of ~25 km in regions with densely distributed stations. The anisotropic model displays structural fabric in relation to surface geologic features such as the Salton Trough, the Transverse Ranges, and the San Andreas Fault. The depth variation of anisotropy does not suggest a lithosphere-asthenosphere decoupling. At long wavelengths, the fast directions of anisotropy are aligned with the absolute plate motion inside the Pacific and North American plates.

1. Introduction

The San Andreas Fault (SAF), the boundary between the Pacific and North American plates, involves a complex system of faults accommodating ~23–37 mm/yr of slip and ~75% of the relative plate motion [*Molnar and Dayem*, 2010]. The pattern of lithospheric deformation and the dynamics of the lithosphere-asthenosphere interaction have persistently been a hot topic of investigation. Seismic anisotropy provides key structural information for studying the mechanics of the SAF system, including the deformations and relative motions of the tectonic blocks, which is critically important for a better understanding of the seismic risks for the entire California region.

There have been numerous studies devoted to isotropic structures of Southern California using body wave traveltimes [*Kohler et al.*, 2003; *Plesch et al.*, 2007], surface wave phase and/or group velocities [*Press*, 1956; *Polet and Kanamori*, 1997; *Tanimoto and Prindle Sheldrake*, 2002; *Yang and Forsyth*, 2006], ambient noise [*Shapiro et al.*, 2005; *Yang et al.*, 2008], and full waveforms [*Chen et al.*, 2007; *Tape et al.*, 2009; *Lee et al.*, 2014]. In contrast, less attention has been paid to the anisotropic structures. A rare exception was the anisotropy tomography of *Monteiller and Chevrot* [2011], although recent surface-wave studies in the western United States [*Yuan and Romanowicz*, 2010; *Yuan et al.*, 2011; *Lin et al.*, 2011] provided a glimpse of regional azimuthal anisotropy with limited lateral and vertical resolution (~70 km).

Shear wave splitting has been one of the primary observables in studying the anisotropy in the crust and upper mantle. However, until recently the interpretation of shear wave splitting in terms of anisotropy has been largely dependent on the ray-theory modeling of a single incident plane wave, in which the shear wave splitting measurements at a station are related to the symmetry axis and strength of anisotropy by a sinusoidal relation:

$$S_i = \delta t \sin 2\left(\phi_f - \phi_b^i\right), \tag{1}$$

where S_i is the splitting intensity at the i-th station whose back azimuth is ϕ_b^i, and ϕ_f and δt are, respectively, the azimuth of the fast axis (the polarization of the fast quasi-shear wave) and the splitting time between fast and slow quasi-shear waves. The pair of the apparent anisotropy parameters, δt and ϕ_f, then prescribes a uniform layer of anisotropy beneath the station, and the splitting of a shear wave varies only with the differential angle $\phi_f - \phi_b^i$. The overly simplified ray-theory assumption of a single plane wave limits the range of source-station geometry in shear wave splitting measurements and reduces our ability to resolve the spatial variations in anisotropy. In this study, we apply a new approach to the inversion of three-dimensional (3D) anisotropy structure based on the full-wave sensitivity (Fréchet) kernels of the splitting data [*Zhao and Chevrot*, 2011a, 2011b; *Lin et al.*, 2014]. The full-wave kernels shown in *Lin et al.* [2014] accurately account for

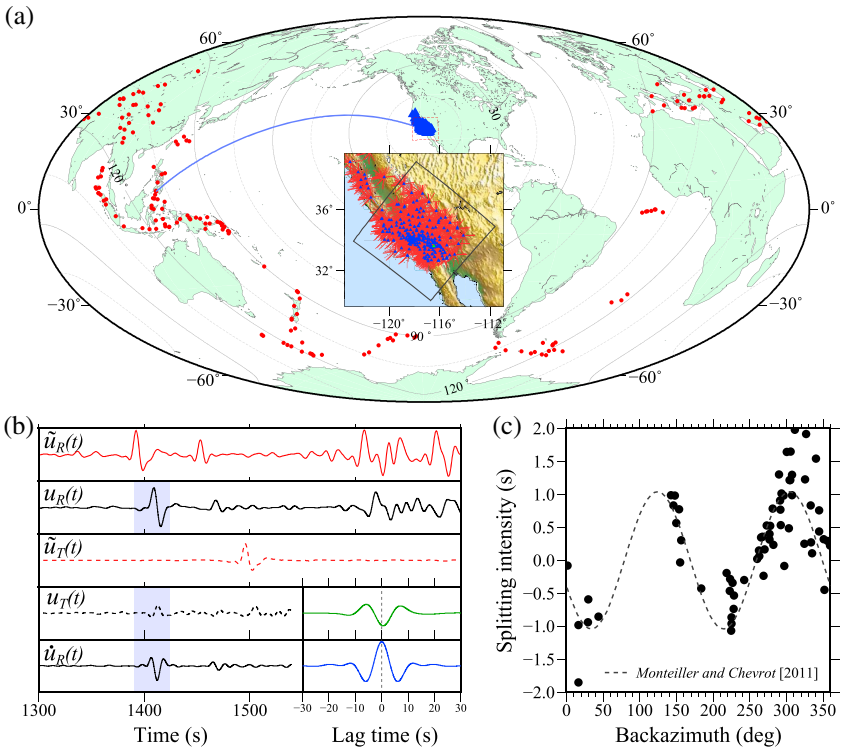

Figure 1. (a) Distributions of stations (blue triangles) and events (red dots). The red bars in the inset panel show the surface projections of the SKS ray paths in the topmost 350 km of the earth beneath the receivers. (b) An example of splitting measurement along the blue great-circle path in Figure 1a. Black and red lines are records and synthetics in PREM, respectively, on radial (solid) and traverse (dashed) components. Shaded zones are the time windows [t_1, t_2] selected for splitting intensity measurements. The bottom right corner shows the cross correlation between $u_T(t)$ and $\dot{u}_R(t)$ (green) and the autocorrelation of $\dot{u}_R(t)$ (blue), while the amplitudes at zero lag time marked by the dashed vertical line give, respectively, the values of the numerator and denominator in equation (2). (c) Individual splitting intensity measurements (black dots) varying with back azimuth at station Pinyon Flat Observatory (PFO) obtained in this study. The dashed curve is the sinusoidal curve that best fits the bin-averaged splitting measurements (not shown here) at PFO from *Monteiller and Chevrot* [2011].

all the wave interactions neglected in ray theory, including near-field effect and interferences of multiple arrivals. *Favier et al.* [2004] used horizontally integrated depth-dependent one-dimensional (1D) kernels in a homogeneous reference model to illustrate the near- and middle-field terms missing in ray theory. Our full-wave approach uses realistic reference models and accounts for the multiple reflections between discontinuities. The resulting depth-dependent sensitivities, as shown in *Lin et al.* [2014], have drastic fluctuations near the surface, especially around the midcrust and Moho discontinuities as a consequence of the combined effects of near-field and multiple reflections in the two crustal layers.

In this study, we use the broadband records at stations in Southern California from globally distributed earthquakes and measure the SKS splittings. We then calculate the full-wave kernels for the splitting data and carry out a multiscale inversion of the anisotropic structure using a wavelet-based model parameterization [*Chiao and Kuo*, 2001; *Chiao and Liang*, 2003; *Chiao et al.*, 2010, 2014]. In addition, we appraise our inversion through a rigorous resolution analysis based on the statistical resolution matrix method of *An* [2012], which provides an effective means to estimate the resolution lengths of the inversion without explicitly calculating the resolution matrix. We also provide an interpretation of our anisotropic model for the Southern California region in terms of geodynamic and geological implications.

2. Splitting Intensity Measurements and Full-Wave Sensitivity Kernels

We measure the SKS splitting intensities using events from 2000 to 2013 with epicentral distances of 90°–130°. Considering a wide range of azimuthal distribution and removing redundancy, records at 223 stations from 175 events (M_W >6) are used in this study (Figure 1a).

Chevrot [2000] demonstrated that the optimal measurement of the shear wave splitting in equation (1) is the splitting intensity, which can be derived from the integral of the product of the SKS signal on the transverse-component $u_T(t)$ and the time derivative of the SKS on the radial component $\dot{u}_R(t)$, i.e., [e.g., *Favier and Chevrot,* 2003; *Chevrot*, 2006]

$$S = -2\frac{\int_{t_1}^{t_2}\dot{u}_R(t)u_T(t)dt}{\int_{t_1}^{t_2}[\dot{u}_R(t)]^2dt}, \tag{2}$$

where $[t_1, t_2]$ is the time window for the shear wave of interest. Considering the dominant periods of the SKS signals and to minimize the interference with neighboring phases, we band pass all waveforms between 0.02 and 0.12 Hz (~50–8 s). To ensure data quality, we manually select the SKS window in each record with a high signal-to-noise ratio and a good similarity between the record and synthetic calculated by normal-mode summation for model PREM [*Dziewonski and Anderson*, 1981]. Following equation (2), we compute the splitting intensity S from the radial- and transverse-component SKS signals. Figure 1b shows an example from a deep event to station Pinyon Flat Observatory (PFO) at a distance of 110.7°. Following a set of strict criteria for data selection, we obtain 5954 splitting intensity measurements. The surface projections of the 5954 SKS ray paths (Figure 1a) manifest an excellent azimuthal coverage.

In conventional SKS splitting analysis assuming a single incident plane wave, the splitting at a station varies with back azimuth in a sinusoidal fashion as shown in equation (1). *Monteiller and Chevrot* [2011] adopted this assumption by averaging individual splitting measurements in azimuthal bins and fitting the bin-averaged values by the sinusoidal curve, which was then used in tomography inversion. From the full-wave point of view, however, SKS often interferes with neighboring phases, leading to a significant contribution to the splitting [*Lin et al.,* 2014]. As a result, the azimuthal variation of the splitting intensity at a station is no longer a sinusoidal function, but rather complex depending on the epicentral distance and even on the earthquake mechanism [*Lin et al.,* 2014]. The full-wave approach accounts for the interferences between SKS and neighboring phases and the near-field effect in the vicinity of station, thus providing the sensitivity kernels of individual splitting intensities to the anisotropic structure. Therefore, individual measurements can be used directly to invert for anisotropy without the need to fit them first by a sinusoidal curve.

Zhao and Chevrot [2011b] and *Lin et al.* [2014] demonstrated that shear wave splitting is mostly sensitive to the parameter $\gamma = (C_{66} - C_{44})/2\rho\beta^2$, where ρ is density, β is the background isotropic S wave velocity, and C_{ij} are elements of the elasticity tensor in the Voigt notation [*Babuška and Cara*, 1991; *Browaeys and Chevrot*, 2004]. *Lin et al.* [2014] also showed that the contributions to shear wave splitting from the other two anisotropy parameters $\varepsilon = (C_{11} - C_{33})/2\rho\alpha^2$ and $\delta = (C_{13} - C_{33} + 2C_{44})/\rho\alpha^2$, where α is the background P wave speed, are less than 10% of that from γ. The model parameters for shear wave anisotropy thus involve γ, a dimensionless parameter describing the strength of shear wave anisotropy [*Mensch and Rasolofosaon*, 1997; *Becker et al.*, 2006; *Chevrot*, 2006], and ϕ_f, the azimuth of the fast axis. The dependence of the splitting intensity S on ϕ_f is, however, nonlinear. *Favier and Chevrot* [2003] defined an alternative set of two independent parameters, $\gamma_c = \gamma \cos 2\phi_f$ and $\gamma_s = \gamma \sin 2\phi_f$, which are linearly related to the splitting intensity:

$$S = \iiint \left[K^S_{\gamma_c}(r,\theta,\phi)\gamma_c(r,\theta,\varphi) + K^S_{\gamma_s}(r,\theta,\varphi)\gamma_s(r,\theta,\varphi)\right] dr d\theta d\varphi, \tag{3}$$

where $K^S_{\gamma_c}$ and $K^S_{\gamma_s}$ are sensitivity kernels of the splitting intensity to γ_c and γ_s, respectively. The values of γ_c and γ_s obtained from the inversion are then used to determine the fast axis and strength of anisotropy through the relations: $\phi_f = 0.5 \tan^{-1}(\gamma_c/\gamma_s)$ and $\gamma = \sqrt{\gamma_c^2 + \gamma_s^2}$. Examples of the 3D sensitivity kernels of S to γ_c and γ_s are shown in Figures 2a and 2b, respectively. For the incoming SKS wave from a back azimuth of 293°, both kernels display banana-doughnut shapes with red and blue "skins" delineating regions of strong sensitivity.

3. Multiscale Inversion

To make the tomography inversion adaptable to spatially varying resolution due to uneven path coverage, we adopt a wavelet-based model parameterization [*Chiao and Kuo*, 2001; *Chiao and Liang*, 2003; *Chiao et al.*, 2010, 2014]. With such scale-adaptive parameterization, the inverse problem can be expressed as:

$$\left(\mathbf{G}\mathbf{W}^{-1}\right)(\mathbf{W}\mathbf{m}) = \mathbf{d}, \tag{4}$$

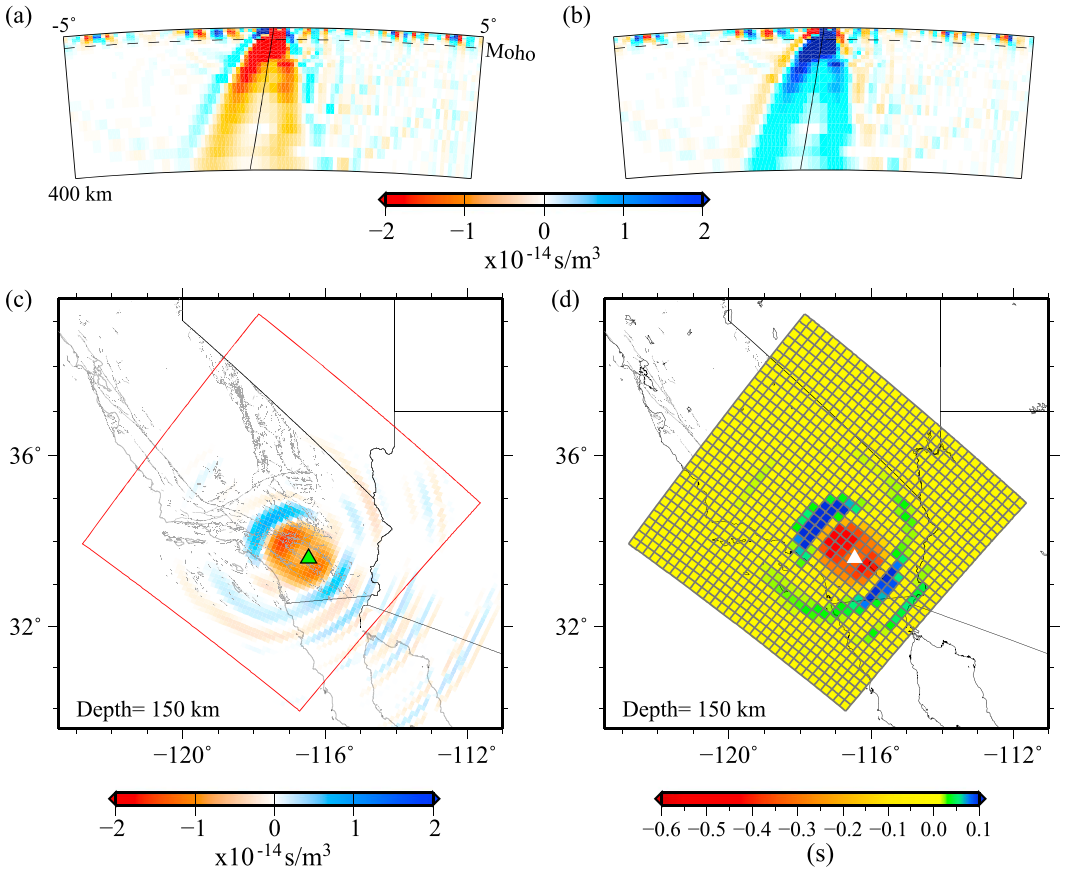

Figure 2. Example of 3D full-wave Fréchet kernels of the splitting intensity for shear wave anisotropy parameters (a) γ_c and (b) γ_s, shown on the source-receiver great-circle plane near the station. Waveforms used to calculate these kernels are displayed in Figure 1b. (c) Map view of the same γ_c kernel in Figure 2a at 150 km depth. The red box depicts the horizontal extent of the anisotropic model to be inverted for. (d) The same kernel in Figure 2c after taking the volumetric integration over individual voxels bounded by the regularly spaced mesh (black lines) subdividing the model by 33 nodes in each dimension. Each voxel-integral value comprises a fraction of a particular element of **G** in equation (4), and the horizontal slice shown in Figure 2d represents a segment of a particular row of **G** corresponding to a splitting intensity measurement obtained at the station shown by the triangle.

where **m** is the vector comprising the model parameters at spatial nodes, **d** is the data vector of splitting measurements, and **G** is the data kernel or Gram matrix. Each element of **G** is associated with a node and contains the weighted sum of the volumetric integrals of the kernel over surrounding voxels (Figure 2d). Matrix **W** represents a 3D wavelet transformation operator. In practice, we first parameterize the model by a 3D uniform mesh, and apply the operator $(\mathbf{W}^{-1})^{\mathrm{T}}$ on each row of **G**. The final model can be obtained by an inverse wavelet transform. Details of the implementation of the multiscale parameterization are well documented by *Hung et al.* [2011]. The wavelet approach preserves both the finer spatial resolution in regions of better data coverage and the coarser resolution in less well-sampled regions, thus resolving the structure with an objective and data-driven multiscale resolution.

Our model has a horizontal dimension of 640 km × 640 km (rotated black box in the inset panel of Figure 1a) and a vertical dimension from the surface down to 350 km depth, which we parameterize by a uniform mesh with 33 nodes in each dimension at 20 km horizontal and 10.9 km vertical spacing. We run inversion experiments using both the wavelet-based model parameterization and the uniform mesh without applying the wavelet transformation. Equation (4) is solved for either **Wm** or **m** using the LSQR algorithm [*Paige and Saunders*, 1982] with a damped least squares solution in which an optimal damping is selected by exploring the trade-off between the model norm and data variance. We choose the optimal damping factors of 10 and 100 corresponding, respectively, to the maximum curvatures of the trade-off curves in the inversions using simple uniform-mesh and wavelet-based model parameterizations (see Figure S1 in supporting information).

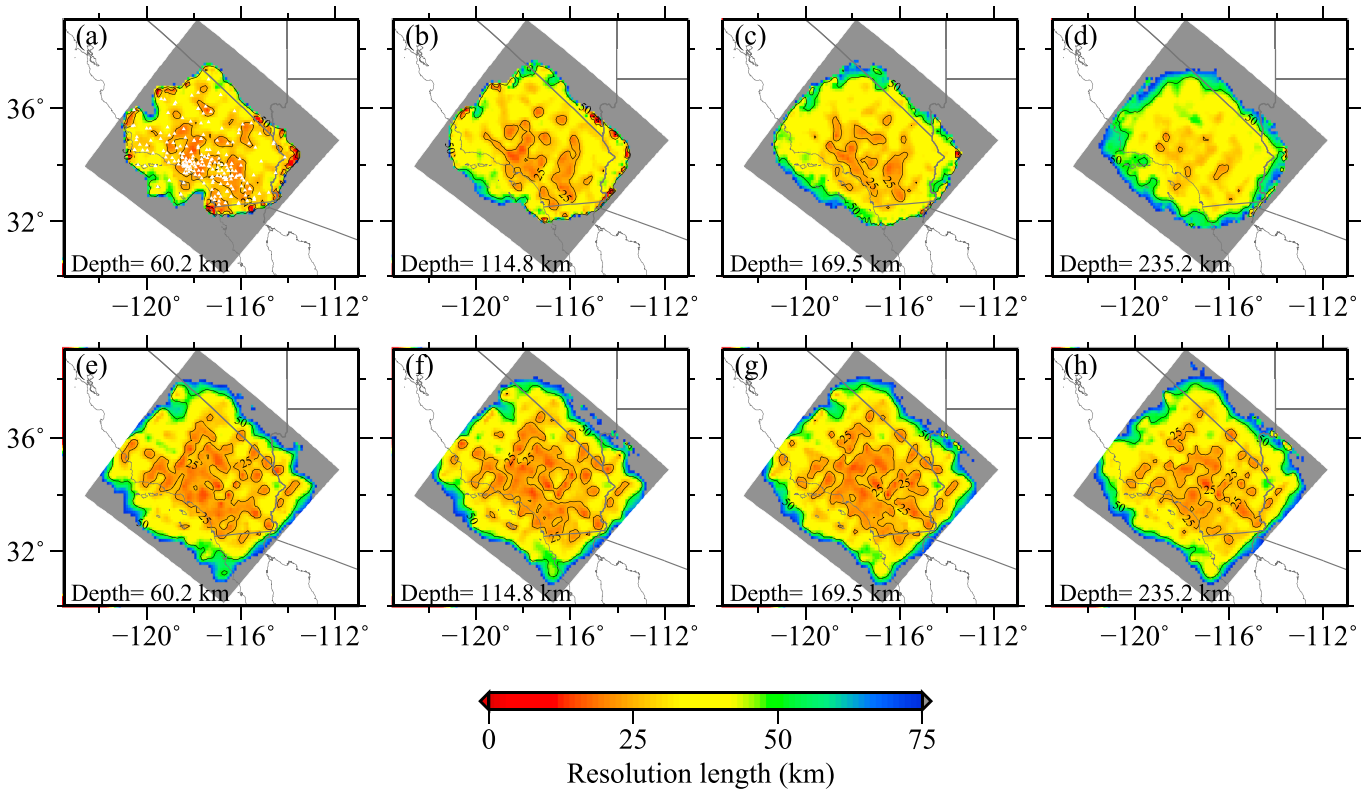

Figure 3. Lateral resolution lengths for γ_c at the depths of (a and e) 60.2 km, (b and f) 114.8 km, (c and g) 169.5 km, and (d and h) 235.2 km, estimated by the statistical resolution matrix method for the 3D model parameterized by regularly spaced nodes (20 km horizontally and 10.9 km vertically) and inverted from ~6000 splitting data. These maps are solved with 300 pairs of random input models and their recoveries using the simple uniform-mesh parameterization with the optimal damping factor 10, and the wavelet-based inversion with damping factor 100. The stations contributing to the splitting measurements are denoted by white triangles in Figure 3a. The γ_c model obtained by wavelet-based multiscale parameterization has shorter resolution lengths and larger resolvable extent than that by uniform-mesh parameterization. The resolution lengths for γ_s are very similar to those for γ_c shown here.

These dimensionless damping factors act differently in the inversions using uniform-mesh and wavelet-based model parameterizations. In the uniform-mesh parameterization, the damping factor is the threshold for removing small singular values of the Gram matrix during the inversion. So the damping acts on the entire model uniformly. For the wavelet parameterization, however, the threshold is imposed on the wavelet coefficients. Larger-scale features are better constrained by the data, and their corresponding wavelet coefficients also have larger singular values than those for smaller-scale features. Furthermore, in regions with better path coverage, more singular values for small-scale wavelet coefficients are above the threshold and retained, while in sparsely sampled regions more singular values for small-scale wavelet coefficients will be damped out. Therefore, the damping affects different regions of the model differently according to the data coverage.

Although the LSQR method provides an efficient means to solve large-scale inverse problems, it proves difficult for obtaining the resolution matrix to appraise the model. Instead of conducting common recovery tests of synthetic models with a few prescribed patterns such as checkerboards, here we adopt the statistical resolution matrix method of *An* [2012] to estimate the resolution lengths of individual model parameters in 3D. Since the resolution matrix does not rely on the data or the model parameters, but on the properties of the data kernel **G**, it can be probed by a limited set of random synthetic models and their recoveries from inversions. As each inverted model parameter can be regarded as the weighted average of the neighboring true model parameters, the resolution matrix comprising these weights is presumed to be a 3D Gaussian function whose unknown width at half of its peak value in each dimension is defined as the resolution length. A finite set of random synthetic models is generated to explore their recoveries obtained by two different means: one from the inversion of model-predictions using the same model parameterization and regularization applied to real data, and the other from the projection of input models via the Gaussian resolution matrix.

The resolution length is then estimated by a grid search for the optimal width minimizing the sum of the absolute difference between the two kinds of recoveries of input models. The statistical resolution matrix approach is very suitable for estimating resolution lengths of large linear inverse problems.

The efficiency and accuracy of the statistical resolution length hinge upon the number of input random models and their inverse solutions. We determine the optimal number of input models by examining the average difference in the resolution lengths of all model nodes derived from two consecutive grid searches for resolution lengths with $N-1$ and N input models. The average differential resolution length drops to ~1% with 299 and 300 synthetic models (see Figure S2 in supporting information). We therefore choose $N=300$ in all our statistical resolution matrix calculations. The resolution-length maps for γ_c displayed in Figure 3 clearly suggest that the wavelet-based inversion yields better and more uniform resolution. They confirm that the wavelet approach preserves a higher resolution in regions of better data coverage and the long-wavelength features in relatively less constrained regions. A bootstrap test is conducted to further validate our inversion result (see Figure S4 in supporting information). A comparison of the observed apparent splitting parameters, i.e., the fast axis ϕ_f and splitting time δt in equation (1), with predictions by our 3D anisotropic model displays highly consistent patterns (see Figure S5 in supporting information). Our following discussion on the anisotropic structure of Southern California will be based on the model obtained by the multiscale inversion.

4. Result and Discussion

Considering the average lithospheric thickness of 70–90 km in Southern California [*Yang and Forsyth,* 2006; *Ford et al.*, 2014] and our vertical resolution length of ~50 km (see Figure S3 in supporting information), we display our model at four depths in Figure 4: one in the lithosphere (60.2 km) and three in the asthenosphere (114.8, 169.5, and 235.2 km). The anisotropy strength ranges in -0.01 to -0.03 (1–3% anisotropy) in this region and slightly decreases with depth. The direction of fast axis varies more dramatically in the lithosphere than in the asthenosphere. At long wavelength, the fast axis exhibits a counter-clockwise rotation from WNW-ESE in the southwest quadrant in the Pacific Plate (PP) to NE-SW in the northeast quadrant in the North American Plate (NAP). Some regions in the lithosphere display a more complex pattern that can be linked to surface geologic signatures (Figure 4a). The fast axis follows a NE-SW orientation west of the Salton Trough, weakens under it, and turns slightly to NW-SE to the east. This variation seems to persist down to the asthenosphere, coincident with the low-velocity anomaly in previous isotropic tomography models, which was interpreted as upwelling beneath the Salton Trough [*Humphreys and Clayton*, 1990; *Yang and Forsyth,* 2006]. A strong E-W fast polarization is observed beneath the Transverse Ranges undergoing active orogenic processes. In the westernmost part of the model, the anisotropy has a more WNW-ESE oriented fast axis, subparallel to the strike of the SAF, and a decreased strength in the lithosphere.

In the asthenosphere, the fast axis in regions more distant from the plate boundary (SAF) correlates well with the absolute plate motion (APM) calculated by the model NNR-MORVEL56 [*Argus et al.*, 2011]. In the easternmost part of our model under the NAP, the fast axes are mostly NE-SW, grossly consistent with the APM of the NAP (~223° azimuth, red arrows in Figure 4). In the westernmost part under the PP, the anisotropy strengthens with depth, and the fast axis turns to WNW-ESE, subparallel to the APM of the PP (~300° azimuth, green arrows in Figure 4). The correlation between the fast axis and APM was also observed in surface-wave azimuthal anisotropy [*Yuan et al.*, 2011; *Kosarian et al.,* 2011]. The persistent E-W fast axes in the asthenosphere across the plate boundary in the center of our model are neither parallel to the APM of the NAP nor the PP, but somewhat in-between, implying an influence by both plates. A small circular region of weak anisotropy (centered around 117°W, 36°N) is resolved throughout all depths, indicative of the presence of a vertical flow there. A possible explanation is that the density-driven mantle flow becomes more vertical beneath the NAP [*Fay et al.,* 2008]. Overall, patterns in the fast axis and anisotropy strength are similar at different depths, while some features are persistent throughout the resolvable depths. Therefore, we do not observe a notable decoupling between the lithosphere and the underlying asthenosphere as reported by some previous studies [*Silver and Holt*, 2002; *Monteiller and Chevrot,* 2011].

Our model exhibits similar anisotropy variations to those in *Monteiller and Chevrot* [2011], except that our model has a weaker anisotropy in the lithosphere, in contrast to their result which showed the strongest strength of anisotropy there. This discrepancy may be explained by the difference in the sensitivity kernels in

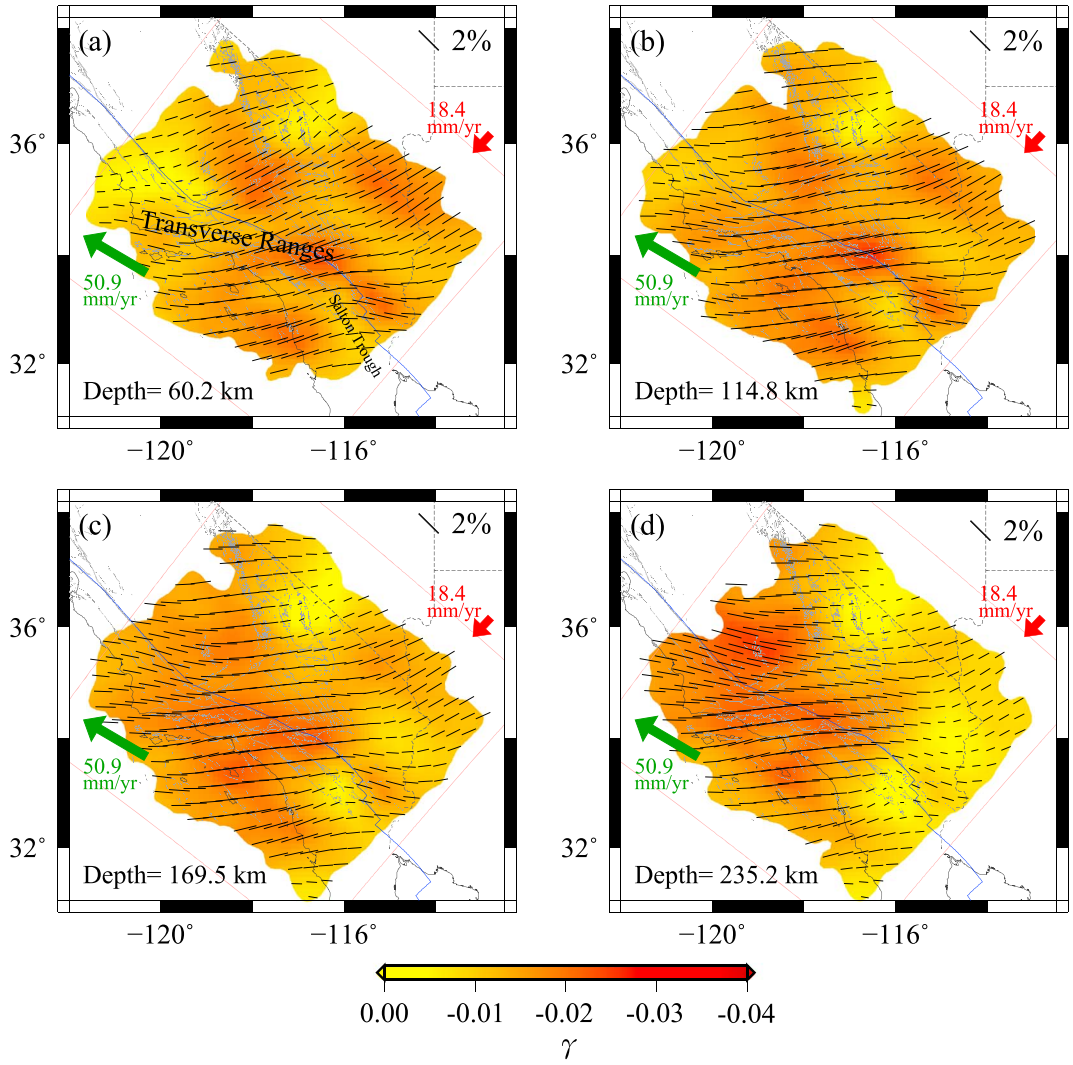

Figure 4. Three-dimensional anisotropy model for Southern California at the depths of (a) 60.2 km, (b) 114.8 km, (c) 169.5 km, and (d) 235.2 km. The background colors indicate the strength of the shear wave anisotropy γ, whereas the black bars depict the directions of the fast axes at every two nodes, and their lengths are proportional to the anisotropy strength. The absolute plate motions (APM) of the Pacific and North America plates, marked, respectively, by the green and red arrows with the lengths proportional to the rates of motion, are calculated by the model NNR-MORVEL56 [*Argus et al.*, 2011]. The plate boundary and fault branches of the San Andreas Fault (SAF) system are shown in the blue and gray lines, respectively.

the two studies. In *Monteiller and Chevrot* [2011] the kernels calculated in a homogeneous model have little sensitivity near the surface and larger values at depth. However, *Lin et al.* [2014] demonstrated that the near-field and multiple reflections between crustal discontinuities drastically change the pattern of the sensitivity, which can be very large around the discontinuities and within the crust. The stronger sensitivities of full-wave kernels at shallow depths thus lead to a weaker strength of the anisotropy there in our model. Another possible reason for the strong anisotropy in the lithosphere in *Monteiller and Chevrot* [2011] is the damping factor imposed in their inversion which increases with depth. *Yuan et al.* [2011] utilized the joint inversion of surface waves and station-averaged apparent splitting data to obtain a 3D azimuthal anisotropic model of the North American upper mantle. Their result exhibits comparable patterns to our model, with E-W fast axes around the plate boundary and rotating to NE-SW beneath the NAP above 150 km depth. Another anisotropic model for western United States obtained by surface wave Eikonal tomography [*Lin et al.*, 2011] also shows the E-W fast axis in the uppermost mantle beneath Southern California. In comparison to those models predominantly relying on surface waves, our inversion of non-averaged individual SKS splitting data yields similar long-wavelength features and at the same time reveals details of the anisotropic structure with higher lateral resolution.

Our multiscale 3D anisotropic model obtained by the full-wave approach, with a resolution length of 25–50 km, reveals the patterns in the strength and fast-axis orientation of anisotropy, a useful probe to infer the state of stress and strain in the lithosphere and the dynamics of the asthenospheric mantle flow around the SAF in Southern California. Local-scale anisotropic fabrics may be associated with surface geologic features, for instance, the possible upwelling beneath the Salton Trough and the ongoing orogeny in the Transverse Ranges. The consistent patterns of anisotropy over depth in our model do not support the notion that the lithosphere is decoupled from the underlying mechanically weaker asthenosphere. The longer-wavelength anisotropic structure suggests that the fast axes in both the PP and NAP are aligned with the APM, whereas in the vicinity of the major plate boundary or the SAF the anisotropy tends to be affected by the motion of both plates. Our approach represents an early step in imaging anisotropy variations. Further developments are needed to adopt numerical wavefield modeling tools such as the spectral-element method [e.g., *Sieminski et al.*, 2007] so that more complex 3D reference models can be used and anisotropic models can be iteratively updated.

Acknowledgments

We thank the Southern California Earthquake Data Center for making its seismic records available to the public. All figures except for Figures 2a and 2b have been generated by the Generic Mapping Tools (GMT) of *Wessel and Smith* [1998]. This research has been supported by the National Science Council of Taiwan under grants NSC102-2116-M-001-013 (Y.-P. L. and L. Z.) and NSC102-2116-M-002-025 (S.-H. H.), and the Academia Sinica, Taipei, Taiwan.

The Editor thanks Sebastien Chevrot and an anonymous reviewer for their assistance in evaluating this paper.

References

An, M. (2012), A simple method for determining the spatial resolution of a general inverse problem, *Geophys. J. Int.*, *191*, 849–864.

Argus, D. F., R. G. Gordon, and C. DeMets (2011), Geologically current motion of 56 plates relative to the no-net-rotation reference frame, *Geochem. Geophys. Geosyst.*, *12*, Q11001, doi:10.1029/2011GC003751.

Babuška, V., and M. Cara (1991), *Seismic Anisotropy in the Earth*, Kluwer Acad., Netherlands.

Becker, T. W., S. Chevrot, V. Schulte-Pelkum, and D. K. Blackman (2006), Statistical properties of seismic anisotropy predicted by upper mantle geodynamic models, *J. Geophys. Res.*, *111*, B08309, doi:10.1029/2005JB004095.

Browaeys, J., and S. Chevrot (2004), Decomposition of the elastic tensor and geophysical applications, *Geophys. J. Int.*, *159*, 667-–678.

Chen, P., L. Zhao, and T. H. Jordan (2007), Full 3D Tomography for the crustal structure of the Los Angeles region, *Bull. Seismol. Soc. Am.*, *97*, 1094–1120.

Chevrot, S. (2000), Multichannel analysis of shear wave splitting, *J. Geophys. Res.*, *105*, 21,579–21,590, doi:10.1029/2000JB900199.

Chevrot, S. (2006), Finite frequency vectorial tomography: A new method for high resolution imaging of upper mantle anisotropy, *Geophys. J. Int.*, *165*, 641–657.

Chiao, L.-Y., and B.-Y. Kuo (2001), Multiscale seismic tomography, *Geophys. J. Int.*, *145*, 517–527, doi:10.1046/j.0956-540x.2001.01403.x.

Chiao, L.-Y., and W.-Z. Liang (2003), Multiresolution parameterization for geophysical inverse problems, *Geophysics*, *68*, 199–209, doi:10.1190/1.1543207.

Chiao, L.-Y., H.-Y. Fang, Y.-C. Gung, Y.-H. Chang, and S.-H. Hung (2010), Comparative appraisal of linear inverse models constructed via distinctive parameterizations (comparing distinctly inverted models), *J. Geophys. Res.*, *115*, B07305, doi:10.1029/2009JB006867.

Chiao, L.-Y., Y.-N. Chen, and Y.-C. Gung (2014), Constructing empirical resolution diagnostics for kriging and minimum curvature gridding, *J. Geophys. Res. Solid Earth*, *119*, 3939–3954, doi:10.1002/2013JB0010364.

Dziewonski, A. M., and D. L. Anderson (1981), Preliminary reference Earth model, *Phys. Earth Planet. Int.*, *25*, 297–356.

Favier, N., and S. Chevrot (2003), Sensitivity kernels for shear wave splitting in transverse isotropic media, *Geophys. J. Int.*, *153*, 213–228.

Favier, N., S. Chevrot, and D. Komatitsch (2004), Near-field influences on shear wave splitting and traveltime sensitivity kernels, *Geophys. J. Int.*, *156*, 467–482.

Fay, N. P., R. A. Bennett, J. C. Spinler, and E. D. Humphreys (2008), Small-scale upper mantle convection and crustal dynamics in southern California, *Geochem. Geophys. Geosyst.*, *9*, Q08006, doi:10.1029/2008GC001988.

Ford, H. A., K. M. Fischer, and V. Lekic (2014), Localized shear in the deep lithosphere beneath the San Andreas fault system, *Geology*, *42*, 295–298, doi:10.1130/G35128.1.

Humphreys, E. D., and R. W. Clayton (1990), Tomographic image of the southern California mantle, *J. Geophys. Res.*, *95*, 19,725–19,746, doi:10.1029/JB095iB12p19725.

Hung, S.-H., W.-P. Chen, and L.-Y. Chiao (2011), A data-adaptive, multiscale approach of finite-frequency traveltime tomography with special reference to P and S wave data from central Tibet, *J. Geophys. Res.*, *116*, B06307, doi:10.1029/2010JB008190.

Kohler, M. D., H. Magistrale, and R. W. Clayton (2003), Mantle heterogeneities and the SCEC reference three-dimensional Seismic Velocity Model Version 3, *Bull. Seismol. Soc. Am.*, *93*, 757–774.

Kosarian, M., P. M. Davis, T. Tanimoto, and R. W. Clayton (2011), The relationship between upper mantle anisotropic structures beneath California, transpression, and absolute plate motions, *J. Geophys. Res.*, *116*, B08307, doi:10.1029/2010JB007742.

Lee, E.-J., P. Chen, T. H. Jordan, P. B. Maechling, M. A. M. Denolle, and G. C. Beroza (2014), Full-3D tomography for crustal structure in Southern California based on the scattering-integral and the adjoint-wavefield methods, *J. Geophys. Res. Solid Earth*, *119*, 6421–6451, doi:10.1002/2014JB011346.

Lin, F.-C., M. H. Ritzwoller, Y. Yang, M. P. Moschetti, and M. J. Fouch (2011), Complex and variable crustal and uppermost mantle seismic anisotropy in the western United States, *Nat. Geosci.*, *4*, 55–61.

Lin, Y.-P., L. Zhao, and S.-H. Hung (2014), Full-wave effects on shear wave splitting, *Geophys. Res. Lett.*, *41*, 799–804, doi:10.1002/2013GL058742.

Mensch, T., and P. Rasolofosaon (1997), Elastic-wave velocities in anisotropic media of arbitrary symmetry-generalization of Thomsen's parameters ε, δ and γ, *Geophys. J. Int.*, *128*, 43–64, doi:10.1111/j.1365-246X.1997.tb04070.x.

Molnar, P., and K. E. Dayem (2010), Major intracontinental strike-slip faults and contrasts in lithospheric strength, *Geosphere*, *6*, 444–467.

Monteiller, V., and S. Chevrot (2011), High-resolution imaging of the deep anisotropic structure of the San Andreas Fault system beneath southern California, *Geophys. J. Int.*, *186*, 418–446.

Paige, C. C., and M. A. Saunders (1982), LSQR: An algorithm for sparse linear equations and sparse least squares, *ACM Trans. Math. Software*, *8*(2), 43–71.

Plesch, A., J. H. Shaw, and C. Benson (2007), Community Fault Model (CFM) for Southern California, *Bull. Seismol. Soc. Am.*, *97*, 1793–1802.

Polet, J., and H. Kanamori (1997), Upper-mantle shear velocities beneath Southern California determined from Long-period surface waves, *Bull. Seismol. Soc. Am.*, *87*, 200–209.

Press, F. (1956), Determination of crustal structure from phase velocity of Rayleigh waves part I: Southern California, *Bull. Geol. Soc. Am.*, *67*, 1647.

Shapiro, N. M., M. Campillo, L. Stehly, and M. H. Ritzwoller (2005), High-resolution surface-wave tomography from ambient seismic noise, *Science*, *307*, 1615–1618.
Sieminski, A., Q. Liu, J. Trampert, and J. Tromp (2007), Finite-frequency sensitivity of body waves to anisotropy based upon adjoint methods, *Geophys. J. Int.*, *171*, 368–389.
Silver, P. G., and W. E. Holt (2002), The mantle flow field beneath Western North America, *Science*, *295*, 1054–1057.
Tanimoto, T., and K. Prindle Sheldrake (2002), Three-dimensional S-wave velocity structure in Southern California, *Geophys. Res. Lett.*, *29*(8), 1223, doi:10.1029/2001GL013486.
Tape, C., Q. Liu, A. Maggi, and J. Tromp (2009), Adjoint tomography of the Southern California crust, *Science*, *325*, 988–991, doi:10.1126/science.1175298.
Wessel, P., and W. H. F. Smith (1998), New, improved version of the Generic Mapping Tools Released, *EOS Trans. Am. Geophys. Union*, *79*, 579.
Yang, Y., and D. W. Forsyth (2006), Rayleigh wave phase velocities, small-scale convection, and azimuthal anisotropy beneath southern California, *J. Geophys. Res.*, *111*, B07306, doi:10.1029/2005JB004180.
Yang, Y., M. H. Ritzwoller, F.-C. Lin, M. P. Moschetti, and N. M. Shapiro (2008), Structure of the crust and uppermost mantle beneath the western United States revealed by ambient noise and earthquake tomography, *J. Geophys. Res.*, *113*, B12310, doi:10.1029/2008JB005833.
Yuan, H., and B. Romanowicz (2010), Depth dependent azimuthal anisotropy in the western US upper mantle, *Earth Planet. Sci. Lett.*, *300*, 385–394.
Yuan, H., B. Romanowicz, K. M. Fischer, and D. Abt (2011), 3-D shear wave radially and azimuthally anisotropic velocity model of the North American upper mantle, *Geophys. J. Int.*, *184*, 1237–1260.
Zhao, L., and S. Chevrot (2011a), An efficient and flexible approach to the calculation of three-dimensional full-wave Fréchet kernels for seismic tomography: I–Theory, *Geophys. J. Int.*, *185*, 922–938.
Zhao, L., and S. Chevrot (2011b), An efficient and flexible approach to the calculation of three-dimensional full-wave Fréchet kernels for seismic tomography: II–Numerical results, *Geophys. J. Int.*, *185*, 939–954.